



HAL
open science

OpenSpyrit: an Ecosystem for Reproducible Single-Pixel Hyperspectral Imaging

Guilherme Beneti Martins, Laurent Mahieu-Williame, Thomas Baudier,
Nicolas Ducros

► **To cite this version:**

Guilherme Beneti Martins, Laurent Mahieu-Williame, Thomas Baudier, Nicolas Ducros. OpenSpyrit: an Ecosystem for Reproducible Single-Pixel Hyperspectral Imaging. *Optics Express*, 2023, 31 (10), pp.15599. 10.1364/OE.483937 . hal-03910077v1

HAL Id: hal-03910077

<https://hal.science/hal-03910077v1>

Submitted on 21 Dec 2022 (v1), last revised 30 Oct 2023 (v2)

HAL is a multi-disciplinary open access archive for the deposit and dissemination of scientific research documents, whether they are published or not. The documents may come from teaching and research institutions in France or abroad, or from public or private research centers.

L'archive ouverte pluridisciplinaire **HAL**, est destinée au dépôt et à la diffusion de documents scientifiques de niveau recherche, publiés ou non, émanant des établissements d'enseignement et de recherche français ou étrangers, des laboratoires publics ou privés.



Distributed under a Creative Commons Attribution 4.0 International License

OpenSpyrit: an Ecosystem for Reproducible Single-Pixel Hyperspectral Imaging

GUILHERME BENETI MARTINS¹, LAURENT MAHIEU-WILLIAME¹,
THOMAS BAUDIER¹, AND NICOLAS DUCROS^{1,*}

¹Univ Lyon, INSA-Lyon, Université Claude Bernard Lyon 1, UJM-Saint Etienne, CNRS, Inserm, CREATIS
UMR 5220, U1294, F-69621, LYON, France

*nicolas.ducros@creatis.insa-lyon.fr

Abstract: This paper describes OpenSpyrit, an open access and open source ecosystem for reproducible research in hyperspectral single-pixel imaging, composed of SPAS (a Python single-pixel acquisition software), SPYRIT (a Python single-pixel reconstruction toolkit) and SPIHIM (a single-pixel hyperspectral image collection). The proposed OpenSpyrit ecosystem responds to the need for reproducibility in single-pixel imaging, which is currently lacking due to limited access to data and reconstruction algorithms. The SPIHIM collection currently contains 140 hypercubes that are acquired using SPAS and reconstructed using SPYRIT. The SPIHIM hypercubes are obtained by inverse Hadamard transformation of the raw data. They have a size of $64 \times 64 \times 2048$ for a spectral resolution of 2.3 nm and a spatial resolution that is comprised between $182.4 \mu\text{m}$ and $15.2 \mu\text{m}$ depending on the digital zoom. We also reconstruct the hypercubes at a resolution of $128 \times 128 \times 2048$ using a data-driven reconstruction algorithm available in SPYRIT, which leads to an increased spatial resolution.

1. Introduction

Spectral imaging is a major tool of modern science, with applications in astronomy, environmental monitoring, food processing, agriculture, and biomedical imaging [1, 2]. The pushbroom and filter-based methods are scanning techniques that require multiple measurements to acquire a full (x, y, λ) hypercube. Pushbroom methods acquire one (y, λ) slice at a time and require scanning along the x -axis [3]. Filter-based setups acquire an (x, y) image for one spectral band, with the full hypercube obtained from a sequence of measurements by rotating a filter wheel or monitoring electronically tunable filters [4]. Both pushbroom and filter-based approaches suffer from low optical throughput as only a small part of the hypercube is measured at a time. Moreover, the spatial (i.e., for pushbroom) or spectral (i.e., for filters) resolutions are linear in proportion to the number of measurements, and hence they are either slow or low resolution. These limitations have led to computational snapshot methods that rely on algorithms that reconstruct a hypercube from a few raw measurements [5]. Coded aperture snapshot spectral imagers and their different variants exploit a diffractive element with a programmable mask, such that each raw measurement gives access to an oblique projection of the hypercube [6]. Miniature ultra-spectral imaging uses a liquid crystal phase retarder to multiplex the spectral domain [7]. The spectral DiffuserCam is a multispectral filter array where the optics are replaced by a diffuser, such that each pixel on the sensor can ‘see’ the whole field of view [8]. However, snapshot imagers suffer from an inherent trade-off between the spatial and the spectral dimensions.

Hyperspectral single-pixel imaging is a generalization of single-pixel imaging whereby a reconstruction algorithm is used to recover high-spectral-resolution hypercubes from a set of spectra obtained using a set of spatial light patterns [9–14]. Compared to snapshot imagers, this approach requires more measurements; however, it leads to an excellent spectral resolution, as the spectral dimension is not multiplexed. Hyperspectral single-pixel imaging traces back to the concept of Hadamard spectroscopy [15] that introduced Hadamard-coded measurements to

46 obtain a signal-to-noise ratio boost known as Fellgett’s effect [16]. This approach has received
 47 renewed interest thanks to the advent of compressed sensing theory that allows the number of
 48 measurements to be drastically reduced [17]. Interest has been further increased with the advent
 49 of deep learning that enables fast reconstruction while outperforming handcrafted prior-based
 50 methods [18]. The number of algorithms that exploit deep learning for single-pixel reconstruction
 51 has continuously increased (see [19–25] to cite only a few relevant works). However, concerns
 52 exist about a number of aspects of algorithms based on deep learning, such as the reliability
 53 of the reconstruction, the dependence on training data, and the ease of interpretation of the
 54 results. There is a need for reproducibility in single-pixel imaging, which is currently lacking
 55 due to limited access to data and reconstruction algorithms. Data-driven algorithms are typically
 56 difficult to compare due to the hyperparameters and stochastic nature of the training phase.
 57 Another concern is the weak characterization of the performance of single-pixel imaging systems
 58 (e.g., resolution, sensitivity, robustness to noise) compared to traditional ones (e.g., pushbroom).
 59 Here, we propose the OpenSpyrit ecosystem for reproducible research in single-pixel imaging.
 60 We have acquired a collection of hypercubes over 2,048 spectral channels using a single-pixel
 61 imaging device whose spectral and spatial resolutions were characterized. Our imaging device
 62 relies on a digital micromirror device (DMD) that displays a sequence of Hadamard patterns. It
 63 acquires a spectrum for each pattern using a commercial spectrometer. While the hypercubes can
 64 be recovered directly by inverse Hadamard transformation of the raw spectra, we also consider an
 65 explainable reconstruction method based on deep learning [21]. Our datasets - SPIHIM [26] - are
 66 made publicly available following FAIR (findability, accessibility, interoperability, reusability)
 67 principles [27]. We share the raw data together with the Hadamard inverse transformed
 68 hypercubes and the hypercubes reconstructed thanks to deep learning. Our reconstruction method
 69 is implemented in the Python package SPYRIT [28], which allows the method to be retrained
 70 from scratch or to evaluate the corresponding Pytorch models that we make available. Our
 71 acquisition software is released via the SPAS package [29]. We believe the OpenSpyrit ecosystem
 72 can considerably ease the training and/or benchmarking of hyperspectral single-pixel image
 73 reconstruction algorithms.

74 2. Methods

75 The computational framework implemented in the OpenSpyrit ecosystem is depicted in Fig. 1.
 76 To acquire a 3D hypercube using a 2D sensor, we acquire multiple pixels at the same time by
 77 shaping the light with a DMD. After a sequence of spectra has been taken by using different
 78 DMD patterns, we feed the raw spectra into a deep reconstruction algorithm that recovers the
 79 hypercube.

80 2.1. Image formation model

Let $\hat{\mathbf{M}} \in \mathbb{R}^{2K \times \Lambda}$ represent the raw measurements, where $2K$ is the number of DMD patterns
 and Λ the number of spectral channels provided by the spectrometer. Let $\mathbf{P} \in \mathbb{R}^{2K \times N}$ be
 the matrix that contains the DMD patterns, where N is the number of (spatial) pixels in each
 pattern and $\mathbf{F} \in \mathbb{R}^{N \times \Lambda}$ represents the 3D hypercube. We model the acquisition process as linear
 measurements corrupted by Poissonian-Gaussian noise [30]

$$\hat{\mathbf{M}} \sim g \mathcal{P}(\mathbf{P}\mathbf{F}) + \mathcal{N}(\mu_{\text{dark}}, \sigma_{\text{dark}}^2), \quad (1)$$

81 where \mathcal{P} and \mathcal{N} are the Poisson and Gaussian distributions, g represents the system gain (in
 82 counts/electron), μ_{dark} is the dark current (in counts), and σ_{dark} is the dark noise (in counts).

We choose \mathbf{P} as Hadamard patterns, which maximizes the signal-to-noise ratio of the
 reconstructed hypercube with respect to the additive Gaussian noise [15]. To handle the negative
 values in \mathbf{P} , the light patterns are split into positive and negative parts to be uploaded onto the

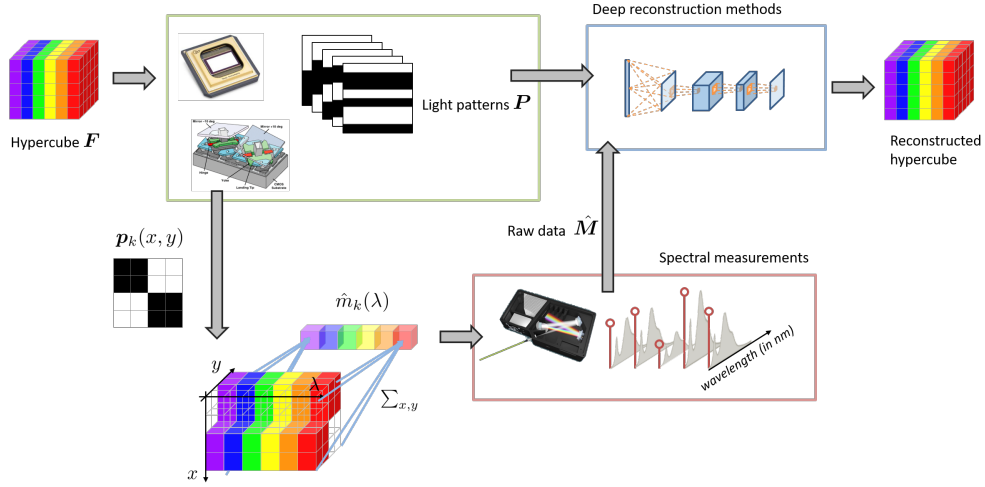


Fig. 1. Hyperspectral single-pixel imaging principle. The hypercube $F \in \mathbb{R}^{N \times \Lambda}$ is sent to a compact spectrophotometer via a digital micromirror device (DMD). A sequence of $2K$ light patterns $P \in \mathbb{R}^{2K \times N}$ is uploaded onto the DMD, leading to the measurement of the $2K$ raw spectra $\hat{M} \in \mathbb{R}^{2K \times \Lambda}$. A reconstruction method is then used to reconstruct the hypercube F from the raw spectra \hat{M} .

DMD [31]. In notations, we have

$$P = \begin{bmatrix} P_+ \\ P_- \end{bmatrix}, \quad (2)$$

where $P_+ \in \mathbb{R}_+^{K \times N}$ and $P_- \in \mathbb{R}_+^{K \times N}$ are the positive and negative parts of Hadamard patterns respectively, i.e., $P_+ - P_- = SH$, where $H \in \mathbb{R}^{N \times N}$ is the Walsh-Hadamard basis and $S \in \{0, 1\}^{K \times N}$ is a subsampling matrix that retains some of the rows of H . In the following, we denote the retained Hadamard patterns by $H_\downarrow = SH$. Different subsampling strategies (e.g., random, low frequency, high variance) have been investigated (see [32] for an overview).

We finally preprocess the raw measurements $\hat{M} = \begin{bmatrix} \hat{M}_+ \\ \hat{M}_- \end{bmatrix}$ to compensate for splitting

$$M = \hat{M}_+ - \hat{M}_-, \quad (3)$$

where $\hat{M}_+ \in \mathbb{R}^{K \times \Lambda}$ and $\hat{M}_- \in \mathbb{R}^{K \times \Lambda}$ correspond to the measurements obtained with the positive and negative patterns, respectively. Therefore, the preprocessed measurements M are Hadamard coefficients, in the sense that $\mathbb{E}(M) = H_\downarrow F$, where \mathbb{E} denotes the expectation. Note that the problem is separable across the spectral dimension, i.e., $\mathbb{E}(m_\lambda) = H_\downarrow f_\lambda$, $1 \leq \lambda \leq \Lambda$, where $m_\lambda \in \mathbb{R}^K$ and $f_\lambda \in \mathbb{R}^N$ are the λ -th column of M and P , respectively. Therefore, the spectral resolution of the hypercube is given directly by the spectral resolution of the spectrometer, while its spatial resolution depends only on the light patterns and our ability to recover f_λ from m_λ .

2.2. Image reconstruction

The hypercube can be reconstructed in the least squares sense as

$$F = \frac{1}{N} H_\downarrow^\top M. \quad (4)$$

In the case $K = N$, the pseudo inverse $\frac{1}{N} H_\downarrow^\top$ is the inverse of H .

We also propose to reconstruct each λ -slice of the hypercube independently by using a data-driven algorithm. We consider the denoised completion network (DC-Net) [33] that computes the two steps

$$\bar{f}_\lambda = \mathcal{G}_{\text{dc}}(\mathbf{m}_\lambda), \quad \text{and} \quad (5a)$$

$$\mathbf{f}_\lambda = \mathcal{D}_\theta(\bar{f}_\lambda), \quad (5b)$$

97 where \mathcal{G}_{dc} represents the denoised completion step and \mathcal{D}_θ represents a neural network with
 98 parameters θ . The denoised completion network is given by $\mathcal{G}_\theta = \mathcal{D}_\theta \circ \mathcal{G}_{\text{dc}}$.

The operator \mathcal{G}_{dc} is chosen as the linear estimator achieving minimum mean squared error under Gaussian assumptions. It is given by

$$\mathcal{G}_{\text{dc}}(\mathbf{m}) = \frac{1}{N} \mathbf{H}_\downarrow^\top \begin{bmatrix} \mathbf{I}_M \\ \boldsymbol{\Sigma}_{21} \boldsymbol{\Sigma}_1^{-1} \end{bmatrix} \boldsymbol{\Sigma}_1 (\boldsymbol{\Sigma} + \boldsymbol{\Sigma}_1)^{-1} \mathbf{m}, \quad (6)$$

where $\mathbf{I}_M \in \mathbb{R}^{M \times M}$ is the identity matrix, $\boldsymbol{\Sigma}_1$ and $\boldsymbol{\Sigma}_{21}$ are blocks of the covariance matrix of $\mathbf{H}\mathbf{f}$ and $\boldsymbol{\Sigma}$ is the noise covariance, which can be estimated as detailed in [21]. While the denoised completion operator \mathcal{G}_{dc} is kept fixed during training, we optimize the parameters of the convolutional neural network in a supervised manner

$$\operatorname{argmin}_\theta \sum_\ell \|\mathbf{f}^{(\ell)} - \mathcal{G}_\theta(\mathbf{m}^{(\ell)})\|^2, \quad (7)$$

99 where $\{\mathbf{f}^{(\ell)} \in \mathbb{R}^N\}_{1 \leq \ell \leq L}$ is an image database and $\{\mathbf{m}^{(\ell)} \in \mathbb{R}^K\}_{1 \leq \ell \leq L}$ are the associated
 100 measurements computed according to Eq. (1) and Eq. (3).

101 2.3. SPAS: Single-Pixel Acquisition Software

102 SPAS [29] is an open source python package for single-pixel acquisition, which has been been
 103 tested to control a DMD 4100 (0.7" XGA VIS, ViALUX) and an AvaSpec-ULS2048CL-EVO
 104 spectrometer. It therefore requires the ALP4lib [34] package for DMD control and the MSL-
 105 Equipment [35] package for spectrometer control. SPAS provides simple functions for the
 106 initialization of the DMD and spectrometer, for the upload of a sequence of patterns into the
 107 DMD memory, and for the acquisition that is triggered by an external signal provided by the
 108 DMD. Each pattern is displayed on the DMD during a given illumination time and the external
 109 trigger is sent to the spectrometer for synchronization. During acquisition, the spectra are stored
 110 in the spectrometer's internal memory and are transferred to the computer via a callback function,
 111 which allows other tasks such as image reconstruction to be run in parallel.

112 SPAS also provides several functions for the visualization of the hypercubes (e.g., spectral
 113 slicing, spectral binning, or RGB representation based on CIE color matching functions [36]),
 114 in addition to the implementation of a simple interface to the more advanced reconstruction
 115 functions of the SPYRIT package (see Section 2.5).

116 2.4. SPIHIM: Single-Pixel Hyperspectral Imaging data collection

117 SPIHIM [26] is a FAIR [27], open-access collection of hypercubes acquired using the principle
 118 of single-pixel imaging. The collection is stored in the PILoT warehouse managed by Girder,
 119 an open source web-based data management platform. Each acquisition is associated with a
 120 uniquely identified folder which contains the raw measurements (`*_spectraldata.npz`),
 121 the hypercube reconstructed by inverse Hadamard transformation (`*_had_reco.npz`), some
 122 metadata (`*_metadata.json`) and an overview folder with several spatial and spectral
 123 representations of the hypercube. The metadata provide information on the experimental

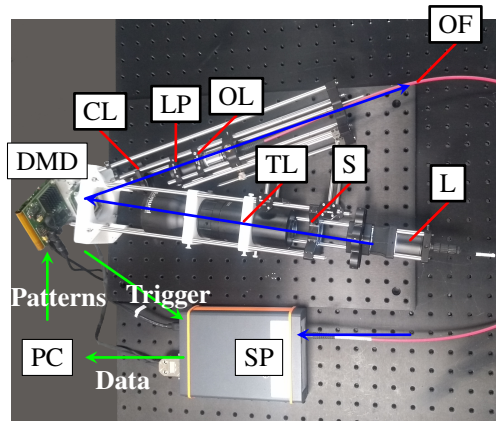


Fig. 2. Acquisition system. Light source (L), sample (S), telecentric lens (TL), digital micromirror device (DMD), bi-convex lens (CL), achromatic lens pair (LP), objective lens (OL), optical fiber (OF), spectrometer (SP), and instrumentation computer (PC). The green arrows indicate the communication workflow between the computer, the DMD, and the spectrometer. The blue arrows indicate the light path.

124 conditions as well as on the acquisition parameters. The collection currently contains 140
 125 hypercubes acquired from 15 different objects: "Star Sector", "Cat", "PpIX", "Color checker",
 126 "USAF", "Colored Star Sector", "No object", "Tomato slice", "Horse", "White spot", "Thorlabs
 127 box", "Blob", "Tree leaf", "Lamb brain", "Apple". For further details about the objects, please
 128 see Section 1A of Supplement 1. We also provide an exhaustive list and detailed description of
 129 the acquisitions made from these objects (see Tables S1-S15 in Supplement 1).

130 2.5. SPYRIT: Single-Pixel Reconstruction Toolkit

131 SPYRIT is a Python package for single-pixel image reconstruction [28] that relies on PyTorch [37]
 132 and can be easily installed using the pip package management system. It implements the forward
 133 model of Eq. (1), the preprocessing step of Eq. (3), and the reconstruction step of Eq. (5)
 134 via classes that inherit from `nn.module`. This allows the full pipeline to be seen from an
 135 image acquisition to its reconstruction as a neural network, in addition to full exploitation of
 136 PyTorch functionalities (e.g., data loaders, network architectures, loss functions, optimizers, etc.).
 137 The source code of the SPYRIT package is available on GitHub and benefits from continuous
 138 integration with automated release of Python packages, dedicated benchmarks for regression
 139 testing, and integrated documentation. The software is licensed under LGPL-3.0: it can be
 140 used and modified by anyone for private, public or commercial use. The SPYRIT package is
 141 complemented by a companion Github repository¹ that contains script examples that rely on
 142 SPYRIT. In particular, the scripts that generate the figures displayed in this manuscript and
 143 Supplement 1 are available in `/2022_OE_spyrit2/`.

144 3. Experiments

145 3.1. Experimental setup

146 Our setup is composed of an illumination arm, a DMD, and a light collection arm as depicted
 147 in Fig. 2. The illumination arm is composed of a white LED lamp (Thorlabs LIUCWHA) and
 148 a bi-telecentric lens system (Edmund Optics TECHSPEC® Large Format Telecentric 62902,

¹<https://github.com/openspyrit/spyrit-examples>

149 magnification 0.9x) that forms the image of the object in the active plane of a DMD (ViALUX
150 GmbH DLP V-700, 1024 x 768 micromirrors, 13.7 μm pitch). The DMD is made of a matrix
151 of microscopic mirrors that can be individually tilted to either $+24^\circ$ (ON state) or -24° (OFF
152 state) according to spatial light patterns. The light collection arm, placed at $+24^\circ$ with respect
153 to the illumination arm, holds a 35 mm focal length bi-convex lens, a MAP104040-B Matched
154 Achromatic Lens Pair (both focal lengths are 40 mm), and an objective lens (x20, NA = 0.35)
155 that focuses light at the entrance of an optical fiber (1500 μm core diameter, NA = 0.39, FT1500
156 UMT) connected to a compact spectrometer (Avantes AvaSpec-ULS2048CL-EVO, $\Lambda = 2048$
157 spectral channels, 515–750 nm, entrance slit of 200 μm , 1200 lines/mm grating). The setup,
158 which is supported by a cage system, is lightweight and transportable. The setup depicted in
159 Fig. 2 is referred to as version v1.1 in the SPIHIM collection. The variants v1.2, v1.3 and v1.3.1
160 differ with respect to the optical elements in the illuminate and collection arms of the setup.
161 Additional details are provided in the SPIHIM collection [26].

162 The integration time of the spectrometer is chosen as equal to the illumination time. A dead
163 time of 44 μs , referred to as dark phase, is necessary for the DMD to tilt its micromirrors
164 according to the next pattern. Another dead time of 356 μs is necessary for the spectrometer to
165 flush its buffer and prepare a new acquisition. This leads to an acquisition time per pattern equal
166 to the spectrometer integration time plus the longest dead time. The total time for the acquisition
167 of a hypercube is $T = 2K(\Delta t + \delta t)$, where Δt represents the integration time and δt represents
168 the dead time. While the integration time can be chosen by the user, the dead time is imposed
169 by the device. Note that the dead time of the spectrometer is much longer than the smallest
170 illumination time allowed by the DMD which cannot be operated at its maximum frequency
171 (22 kHz corresponding to 45 μs). Our acquisitions are typically made with an integration time
172 of 1 ms. Therefore, the fully sampled acquisition of an image of $N = 64 \times 64$ pixels requires
173 $2K = 2N = 8,192$ patterns $\times 1.4 \text{ ms} \approx 11.5 \text{ s}$.

174 3.2. Experimental data for setup characterization

175 For the purpose of reproducibility, we characterize the spatial and spectral resolution of the
176 setup. To do so, we consider five objects from the SPIHIM collection. To determine the spatial
177 resolution, we consider the Star Sector resolution target (Thorlabs, R1L1S2P, see top row of
178 Fig. 4) and the USAF resolution target (Edmund, USAF 1951 38256, see bottom row of Fig. 4).
179 Both samples are illuminated in transmission using a cold white LED array light source (Thorlabs,
180 LIUCWHA). To determine the spectral resolution, we consider the light spots of a Mercury-Argon
181 calibration lamp (Ocean Optics HG-1 with characteristic peaks at 546, 577, 579, 697, 707, 727,
182 and 738 nm). As a more realistic reference image, we consider the image of a cat taken from the
183 STL-10 [38] test set. The cat image is printed on a plastic sheet on which we superimpose a linear
184 variable filter (Ocean Optics, LVF-HL, see Fig. 3). Finally, we consider an image of a tomato
185 slice (see Fig. 7) to evaluate the capacity of the neural network to reconstruct the hypercube
186 as a function of the acceleration rate. A tomato slice has smooth optical contrast compared to
187 calibration targets that have high symmetry and sharp edges where reconstruction can fail for an
188 undersampled acquisition. Details about these acquisitions can be found in Supplement 1 (see
189 Tables S1, S2, S5, S7 and S8).

190 Irrespective of the imaging configuration, all the patterns of a 64×64 Hadamard basis are
191 acquired, resulting in a total of $K = N = 4,096$ Hadamard patterns split into 8,192 positive and
192 negative patterns. We also consider accelerated acquisitions for which $K < 4,096$ patterns are
193 acquired. The fully sampled datasets can be downsampled *a posteriori* to simulate an accelerated
194 acquisition with different acceleration factors. Typically, the 64×64 Hadamard patterns are
195 resized to fill the largest square region possible on the DMD, which corresponds to 768×768
196 micromirrors. In this case, each pixel of the Hadamard patterns corresponds to an area of 12×12
197 micromirrors. However, it is also possible to display the patterns on smaller fields of view, acting

Table 1. Integration times for the different zooms and samples. Times are given in ms/pattern; ‘n.a.’ indicates that a dataset is not available. The corresponding images are available in Supplement 1 (see Tables S1, S2, S5, S7 and S8). Click on the integration times to access the raw data via a unique identifier.

Zoom	×1	×2	×3	×4	×6	×12
Pixel size (μm)	182.4	91.2	60.8	45.6	30.4	15.2
STL-10 cat	1	n.a.	n.a.	n.a.	n.a.	n.a.
Star Sector	1	4	9	16	36	144
USAF	1	4	9	16	36	144
Mercury-Argon lamp	17.4	n.a.	n.a.	n.a.	n.a.	n.a.
Tomato slice	1	4	n.a.	n.a.	36	144

198 as a hardware zoom that is independent of the optical components of the acquisition setup. We
 199 consider six DMD-based hardware zooms: ×1, ×2, ×3, ×4, ×6, and ×12, which correspond
 200 to patterns with a pixel size of 12, 6, 4, 3, 2, and 1 micromirrors, respectively. The higher the
 201 zoom factor, the lower the photon counts. To obtain measurements with similar signal-to-noise
 202 ratios, we chose the integration time depending on the zoom, as indicated in Table 1. For the ×1
 203 zoom, we set the integration time to 1 ms/pattern for the STL-10 cat and 17.4 ms/pattern for the
 204 Mercury-Argon calibration lamp. For the Star Sector and USAF targets that we image at zooms
 205 ×1, ×2, ×3, ×4, ×6, and ×12, we choose integration times of 1, 4, 9, 16, 36, and 144 ms/pattern,
 206 respectively. For the tomato slice, we choose 4 ms/pattern for ×2 zoom and 144 ms/pattern for
 207 ×12 zoom.

208 3.3. Training of the DC-Net

209 We train a DC-Net using SPYRIT [28] for a number of measurements of 4096, 2048, 1024,
 210 and 512. In particular, we consider the $L = 100,000$ images that correspond to the ‘test’
 211 subset of the ImageNet dataset [39]. The original images are randomly cropped to 128×128
 212 and are normalized between -1 and 1 . The image domain denoiser \mathcal{D}_θ is a U-Net with three
 213 downsampling steps separated by a max pooling operation and three upsampling steps separated
 214 by transposed convolutions. The number of filters in the contracting path is increased from 16 to
 215 32, then to 64. Each layer is separated by a ReLU and batch normalization layer. Our U-Net has
 216 a total of 499,985 learnable parameters. We solve Eq. (7) using the ADAM optimizer [40], with
 217 an initial learning rate of 10^{-3} , which is halved every 10 epochs, for a maximum of 30 epochs.
 218 The training phase took about 300 minutes on a NVIDIA GeForce RTX 2080 Ti graphic card in
 219 the case of $K = 512$. The DC-Nets trained for the four number of measurements are available in
 220 the /soft/model/ folder of SPIHIM. They can be easily loaded and run using SPYRIT (see
 221 Section 2 of Supplement 1 for a comprehensive overview of the hypercubes reconstructed for
 222 different numbers of measurements).

223 4. Results

224 4.1. An acquisition example

225 To show the spatial and spectral capabilities of our hyperspectral camera, we first consider the
 226 STL-10 cat image with a linear variable filter in front of it. The integration time was set at 1
 227 ms/pattern leading to a total acquisition time of 11.5 s. Figure 3 shows the obtained hypercube
 228 to which we apply spectral binning to facilitate its display. We compute seven bins within the

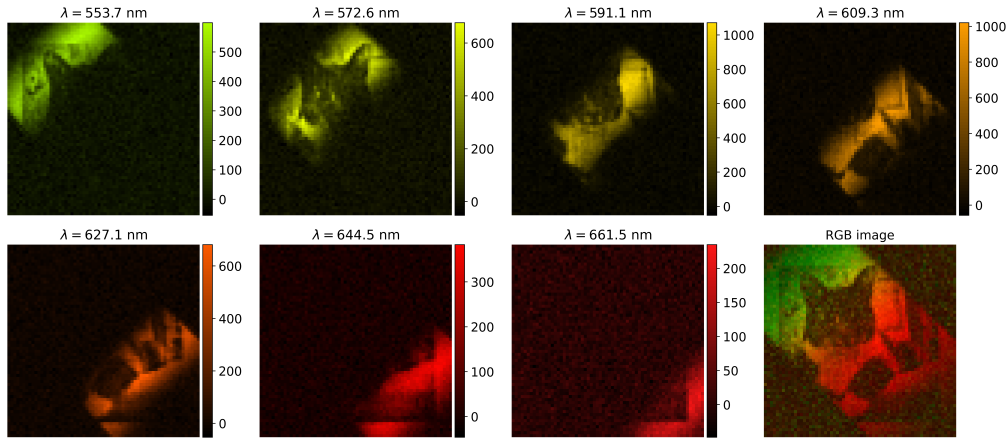


Fig. 3. STL-10 cat hypercube acquisition with a linear variable filter. The full hypercube is binned spectrally for display (seven bins in the range 544–670 nm, bin widths ~ 19 nm, central wavelengths: 553.7, 572.6, 591.1, 609.3, 627.1, 644.5, and 661.5 nm). The colorbars show intensities in counts/pixel. The image on the bottom right is an RGB representation of the full hypercube. Acquisition: $K = N = 4,096$ patterns, $\times 1$ zoom, integration time of 1 ms/pattern; reconstruction by means of Eq. (4) with $N = 4,096$.

229 544–670 nm range with a bin width of ~ 19 nm (central wavelengths: 553.7, 572.6, 591.1, 609.3,
 230 627.1, 644.5, and 661.5 nm). We also provide an RGB representation as recommended by the
 231 CIE [36]. Details about this acquisition can be found in Supplement 1 (see Table S2).

232 Each bin displays a different bandpass window that is selected by the linear filter. As expected,
 233 the bandpass window translates diagonally within the field of view, from the top left corner to
 234 the bottom right corner, as the central wavelength increases. This is also visible on the RGB
 235 representation that displays the color palette starting with the green color in the top left corner to
 236 the red color in the bottom right corner. The STL-10 cat is visible in the background.

237 4.2. Spatial resolution and DMD-based zoom

238 We evaluate the spatial resolution of our system by imaging two calibrated resolution targets: the
 239 Star Sector and the USAF target. The Star Sector is composed of 36 black bars distributed around
 240 360° . The USAF target is composed of bar groups with decreasing bar spacing and length. In
 241 Fig. 4, we display the images obtained for both targets at four different zooms ($\times 1$, $\times 3$, $\times 6$, and
 242 $\times 12$), after summation in the 550–590 nm range. The integration time was set at 1, 9, 36, and
 243 144 ms/pattern respectively leading to a total acquisition time of 11.5, 77.0, 298.2, and 1,183.0 s
 244 respectively. Details about these acquisitions can be found in Supplement 1 (see Tables S1 and
 245 S5).

246 For both targets, we first establish the spatial resolution in pixels. Then, we convert it to line
 247 pairs per millimeter (lp/mm) to account for the optical magnification. For the Star Sector, we
 248 determine the system resolution as the smallest radius of a circular profile for which consecutive
 249 black bars appear to touch. For the USAF, we determine the system resolution as the smallest
 250 distinguishable bar group vertically and horizontally [41]. We also report the theoretical spatial
 251 resolution computed as $1/(2\Delta x)$, where Δx is the image pixel size in millimeters. The image
 252 pixel size depends linearly on the zoom, given the DMD pixel size and the telecentric lens
 253 magnification. We obtain 182.4, 91.2, 60.8, 45.6, 30.4, and 15.2 μm for $\times 1$, $\times 2$, $\times 3$, $\times 4$, $\times 6$, and
 254 $\times 12$ zooms, respectively (see Table 1).

255 In Fig. 5, we plot the spatial resolution as a function of the zoom, considering six different

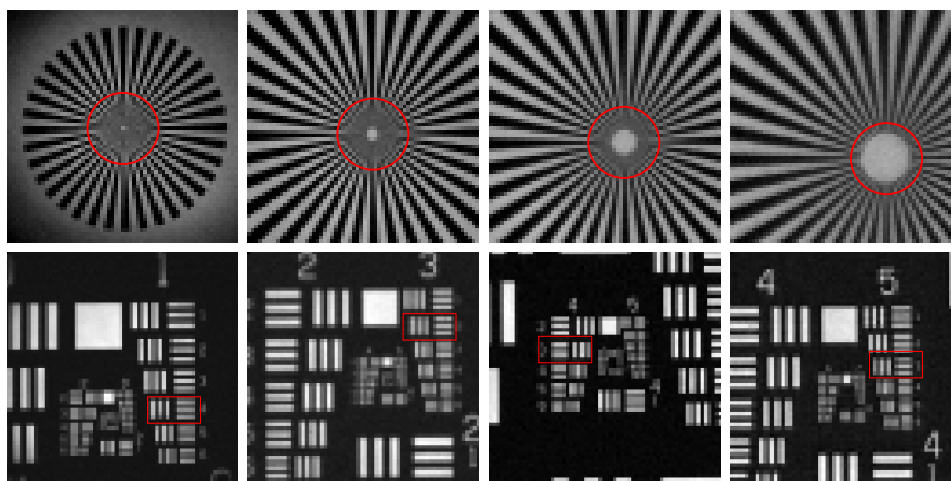


Fig. 4. Resolution targets acquired with different zooms. Top row: Star Sector; bottom row: USAF. Zoom increases from left to right: $\times 1$, $\times 3$, $\times 6$, and $\times 12$; $K = N = 4,096$ patterns; the integration time increases with the zoom: 1, 9, 36, and 144 ms/pattern, from left to right. All hypercubes are reconstructed using Eq. (4). The displayed images are obtained by summing the hypercubes in the 550-590 nm range.

256 zooms that correspond to six independent acquisitions. We observe that spatial resolutions
 257 obtained from both the USAF and Star Sector targets are in good agreement with theoretical
 258 values computed from the pixel size only. This indicates that our system is limited only by the
 259 pixel size and that the DMD-based hardware zoom is not associated with undesirable blur.

260 4.3. Spectral resolution at different locations

261 We evaluate the spectral resolution by imaging a Mercury-Argon calibration lamp positioned
 262 in the object plane. We place the lamp at three different positions to create light spots at
 263 different locations in the field of view and acquire a hypercube for each spot. Figure 6 shows the
 264 superposition of the three lamp spots ($2K = 8,192$ patterns per acquisition, integration time $\Delta t =$
 265 17.4 ms/pattern). Details about this acquisition can be found in Supplement 1 (see Table S7).

266 For all three acquisitions we observe a central bright spot corresponding to the position of the
 267 light source (Fig. 6(a)). For each spot, we sum the contributions of all pixels in the respective red
 268 rectangles, obtaining the spectra indicated in Fig. 6(b). For the three acquisitions, we recover a
 269 spectrum that consists of the emission lines of mercury ($\lambda < 650$ nm) and argon ($\lambda > 650$ nm).
 270 In the following, we consider the peaks at 546, 697, 707, 727, and 738 nm. We measure the full
 271 width at half maximum of all peaks, for all spot locations, and obtain spectral resolutions between
 272 2.15 nm and 2.30 nm. These spectral resolutions are in excellent agreement with the theoretical
 273 spectral resolution of the spectrometer that is 2.3 nm, confirming that the spectral resolution of
 274 our device is directly given by the spectral resolution of the spectrometer. We observe no spectral
 275 degradation that originates from components before the spectrometer (e.g., DMD or focusing
 276 optics). Note that the peak at 578 nm results from the observation of the mercury emission
 277 doublet at 577 and 579 nm, which cannot be resolved. We also find that the amplitude of the
 278 different peaks, except the doublet, are the same for the three spot locations, which indicates that
 279 the spectral response of our system is spatially invariant.

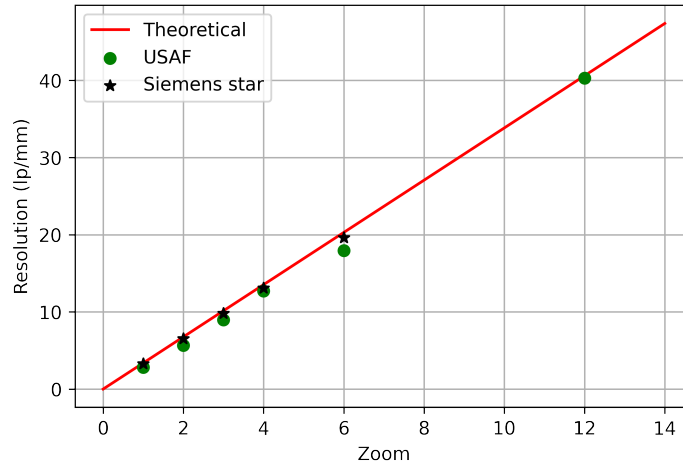


Fig. 5. Spatial resolution as a function of the zoom. The red line is the theoretical resolution calculated from the pixel size; the green dots represent the resolution measured from the USAF target; the black stars represent the resolution measured from the Star Sector target. The spatial resolution is given in line pairs/millimeters (lp/mm) and evaluated from the images displayed in Fig. 4.

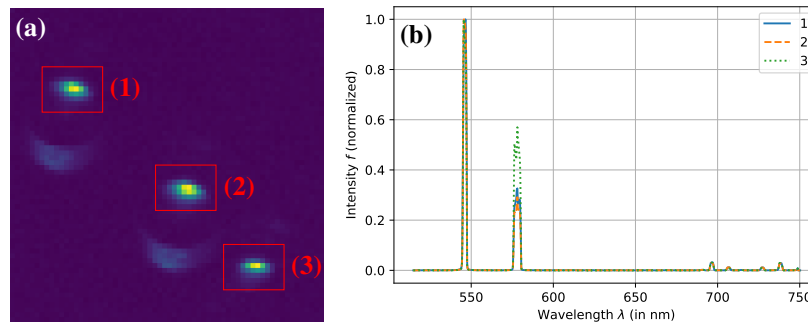


Fig. 6. Spectral resolution at different spatial locations in the field of view. (a) Image of a three-spot of the Mercury-Argon calibration lamp. (b) Spectra of each of the light spots indicated in (a). Integration time: 17.4 ms/pattern. The image in (a) is obtained by summing the hypercube along the spectral dimension. The spectra in (b) are obtained by summing all pixels within the red rectangles displayed in (a). These results confirm that the spectral resolution of our device is directly given by the spectral resolution of the spectrometer and that the spectral response of our system is spatially invariant.

280 4.4. Reconstructions for different values of K and N

281 We evaluate our ability to reconstruct images from different amounts of measurements considering
282 three samples: the Star Sector target, the USAF target, and a tomato slice. We consider the Star
283 Sector and USAF targets imaged using $\times 12$ zoom, whereas for the tomato slice, both the $\times 2$ and
284 $\times 12$ zooms were considered. Details about these acquisitions can be found in Supplement 1
285 (see Tables S1, S5 and S8). For each sample, we consider $K = 4,096$ measurements, $K = 1,024$
286 measurements, and $K = 512$ measurements. The case $K = 4,096$ measurements corresponds to a
287 full basis scan with 64×64 Hadamard patterns. The cases $K = 1,024$ and $K = 512$ measurements
288 are obtained by subsampling the full basis scan acquisition. We retain the patterns that lead to
289 the measurements with the highest energy (i.e., we chose \mathbf{S} such that $\mathbb{E}(\|\mathbf{SHf}\|_2^2)$ is maximal),
290 as suggested in [42]. We reconstruct the hypercubes in the least square sense using Eq. (4) (see
291 first column of Fig. 7) as well as with the data driven DC-Net given by Eq. (5) (see second,
292 third, and fourth columns of Fig. 7). All reconstructed images are obtained by keeping a single
293 spectral channel at $\lambda = 579$ nm. The Hadamard matrices are constructed such that the set of
294 patterns at a given resolution is included in the set of patterns at higher resolutions. For instance,
295 a full basis scan at resolution 64 (i.e., $K = 4,096$ measurements taken from patterns of size
296 $N = 64 \times 64$) is equivalent to an acquisition at resolution 128 (i.e., $K = 16,384$ measurements
297 taken from patterns of size $N = 128 \times 128$) undersampled by a factor of four. To illustrate this, we
298 reconstruct the USAF target at resolution 64 (see second row of Fig. 7) and at resolution 128 (see
299 third row of Fig. 7). More hypercubes reconstructed at resolution 128 can be found in Section 2
300 of Supplement 1 where we consider fifteen different objects and four different spectral channels.

301 The least-squares reconstruction is independent of the choice for N and depends on K only,
302 which can be seen by comparing the first image of the second row and the first image of the third
303 row. On the other hand, the reconstruction quality of the data-driven algorithm depends on the
304 size of the images considered during the training phase. Training the DC-Net with 128×128
305 images rather than with 64×64 images improves the quality of the reconstruction significantly.
306 This can be observed by comparing the images of the second row of Fig. 7 to those of the third
307 row of Fig. 7. In particular, the bars of the elements 5 and 6 of the group 4 can be resolved in the
308 deep reconstruction, but not in the least-squares reconstruction (see the red rectangles in Fig. 7).
309 This improvement is observed even if no such piecewise-constant binary images are present in the
310 ImageNet database used for training. As expected, lowering the number of measurements leads
311 to a loss of spatial resolution, which can be evaluated from the reconstructions of the resolution
312 targets (see second, third, and fourth rows of Fig. 7). The lower the number of measurements, the
313 higher the loss. For the Star Sector, the degradation of the spatial resolution appears as a blurred
314 region in the center of the target, where high spatial frequency structures are present. We also
315 observe this effect in the tomato slice images (see fifth and sixth row of Fig. 7). However, as
316 fewer high frequencies are present, the degradation appears more limited.

317 5. Discussion

318 Images collected by hardware-driven commercial systems are relatively abundant. Among
319 the main hyperspectral databases, the AVIRIS collection (e.g., see the NASA website [43])
320 contains thousands of hypercubes over 214 spectral channels taken from airborne platforms.
321 The BGU ICVL collection [44] currently contains 201 hypercubes over 519 spectral channels
322 corresponding to indoor and outdoor scenes taken from the ground. Very few databases offer
323 hypercubes with more than a thousand spectral bands. In contrast to existing datasets, our
324 computational device provides access to 2,048 spectral channels. Our imaging system natively
325 acquires a $64 \times 64 \times 2048$ hypercube with a spectral resolution of 2.3 nm, while the spatial
326 resolution can be adjusted between $182 \mu\text{m}$ and $15 \mu\text{m}$ using a DMD-based hardware zoom that
327 can achieve a $\times 12$ magnification with no modification of the optical components. The setup
328 characterization demonstrates that the spectral resolution is not affected by the micromirror matrix

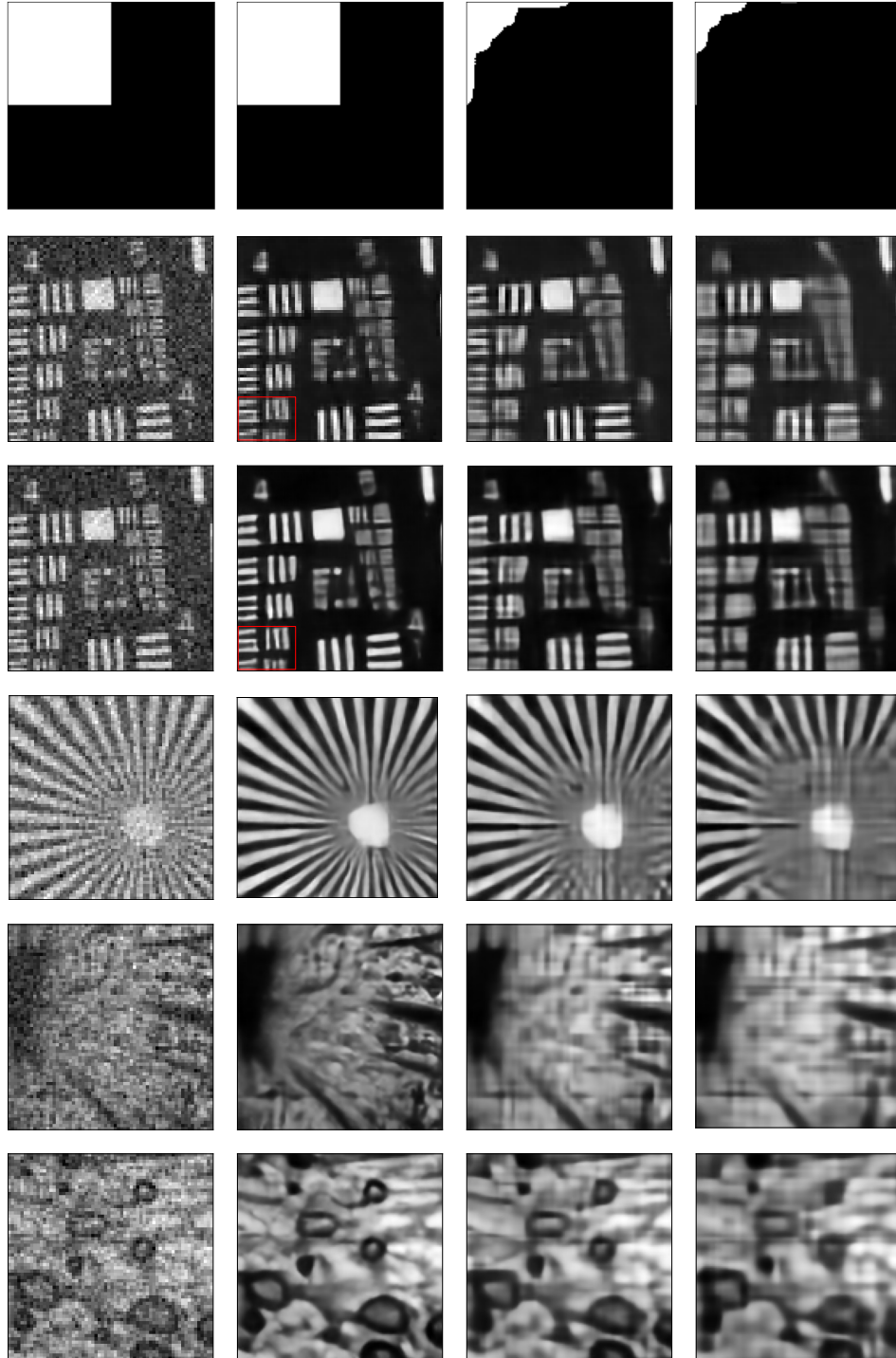


Fig. 7. Image reconstructions for different samples, number of measurements, and reconstruction methods. First row: subsampling masks for $N = 128 \times 128$; second and third rows: USAF $\times 12$ zoom; fourth row: Star Sector $\times 12$ zoom; fifth row: tomato slice $\times 2$ zoom; sixth row: tomato slice $\times 12$ zoom. First column: $K = 4,096$ measurements, least-squares reconstruction; second column: $K = 4,096$ measurements, denoised completion network (DC-Net) reconstruction; third column: $K = 1,024$ measurements, DC-Net reconstruction; fourth column: $K = 512$ measurements, DC-Net reconstruction. The least-squares reconstructions are obtained using Eq. (4), while the DC-Net reconstructions are given by Eq. (5). We have set $N = 128 \times 128$ in all rows, except in the second where $N = 64 \times 64$. All images correspond to the spectral channel $\lambda = 579$ nm.

329 of the DMD and is equal to that of the commercial spectrometer, while the spatial resolution is
330 approximately driven by the minimal group of micromirrors. As for the optical zoom, the higher
331 the magnification, the lower the photon flux. To account for this effect, the images at higher
332 zooms have been acquired for a longer duration (see Fig. 4), with a scaling factor equivalent
333 to the zoom squared. Our system maintains a high spectral resolution for a lower price than
334 currently available hyperspectral cameras with the same spectral resolution.

335 The shortest integration time that we consider is 1 ms/pattern, leading to a total acquisition
336 time of 11.5 s. As the spectrometer imposes a dead time δt of 356 μ s during which no signal is
337 acquired, this represents a waste of $356/(356 + 1000) \approx 26\%$ of the total acquisition time. To
338 reduce the total acquisition time, it is possible to reduce the number of patterns $2K$ uploaded onto
339 the DMD. The total acquisition time of the accelerated acquisition depends directly on the number
340 of patterns (e.g., $11.5/2 \approx 5.75$ s considering only half of the patterns). This acceleration comes
341 at the cost of a spatial resolution reduction, as illustrated in Fig. 7. The acceptable acceleration
342 factor depends on the frequency content of the scene. While a 2-fold acceleration may be already
343 excessive for sharp or highly structured objects, an acceleration up to 8-fold may be acceptable
344 for smoother objects. In this study, we chose a subsampling strategy based on energy criteria;
345 however, any other subsampling strategy can be evaluated by subsampling a full acquisition a
346 posteriori. The determination of the best subset of patterns remains an open problem and the
347 subject of active research. To ease such studies, we provide several examples for reading and
348 reordering the SPIHIM measurements according to a given subsampling pattern as done in Fig. 7.

349 For the sake of generality, we have chosen to provide reconstructions where no assumptions
350 are made on the spectral content of the hypercube. Therefore, our algorithm reconstructs each
351 λ -slice of the hypercube independently using a DC-Net. We have chosen this approach for its
352 robustness to noise deviation, as underlined in [21]. However, many other data-driven approaches
353 can be considered, including approaches that exploit the spatio-spectral redundancy to jointly
354 reconstruct several λ -slices (e.g., [45]). The OpenSpyrit ecosystem could serve as a basis for a
355 more systematic comparison of the performance of these algorithms. Alternatively to the splitting
356 strategy given by Eq. (2), the patterns can be shifted to positive values. While the comparison of
357 shifting and splitting have been addressed in [31] for wavelet patterns, the question of handling
358 the negative values of Hadamard patterns remains open. The SPIHIM collection allows studies
359 to be conducted with both approaches. Indeed, shifted Hadamard patterns $\frac{1}{2}(SH + 1)$ coincide
360 with the positive part of Hadamard patterns P^+ . Therefore, the SPIHIM collection includes
361 the measurements from shifted Hadamard patterns that are obtained by retaining every second
362 spectrum.

363 6. Conclusion

364 We propose OpenSpyrit, an ecosystem for reproducible research in hyperspectral single-pixel
365 imaging. In particular, we introduce SPAS (a Python acquisition package), SPYRIT (a Python
366 reconstruction package) and SPIHIM (a data collection), to respond to the need for reproducibility
367 and open access in single-pixel imaging. The SPIHIM collection currently contains 140
368 hypercubes that are natively $64 \times 64 \times 2048$ in size with a spectral resolution of 2.3 nm and a
369 spatial resolution that can be adjusted between 182.4 μ m and 15.2 μ m using a digital zoom. It
370 also contains the hypercubes reconstructed at resolution of $128 \times 128 \times 2048$ by a data-driven
371 reconstruction algorithm. The SPIHIM dataset can be exploited for spectral imaging studies
372 in general, but also for more specific studies. In particular, the OpenSpyrit ecosystem should
373 provide a benchmark for single-pixel reconstruction algorithms. In the future, the data collection
374 is expected to continue growing and, in a similar manner, the SPYRIT package should integrate
375 novel reconstruction algorithms.

376 **Funding.** This study was supported by the French National Research Agency (ANR), under Grant
377 ANR-17-CE19-0003 (ARMONI Project), and performed within the framework of the LABEX PRIMES
378 (ANR-11-LABX-0063) of Université de Lyon. It received the support of the CNRS through the PNRIA

379 Program.

380 **Acknowledgments.** Part of this work is based on acquisitions achieved on the PILoT facility, member of
381 the infrastructure France Life Imaging (ANR-11-INBS-0006). N.D. would like to thank Antonio Lorente
382 Mur for the many fruitful discussions on reconstruction strategy.

383 **Disclosures.** The authors declare that they have no conflicts of interest.

384 **Data availability.** Data underlying the results presented in this paper are available in the SPIHIM
385 collection of the PILoT warehouse [26].

386 **Supplemental document.** See Supplement 1 for supporting content.

387 References

- 388 1. B. Boldrini, W. Kessler, K. Rebner, and R. W. Kessler, "Hyperspectral Imaging: A Review of Best Practice,
389 Performance and Pitfalls for in-line and on-line Applications," *J. Near Infrared Spectrosc.* **20**, 483–508 (2012).
- 390 2. Q. Li, X. He, Y. Wang, H. Liu, D. Xu, and F. Guo, "Review of spectral imaging technology in biomedical engineering:
391 Achievements and challenges," *J. Biomed. Opt.* **18**, 100901 (2013).
- 392 3. A. F. H. Goetz, "Three decades of hyperspectral remote sensing of the Earth: A personal view," *Remote. Sens.*
393 *Environ.* **113**, S5–S16 (2009).
- 394 4. J. W. Lichtman and J.-A. Conchello, "Fluorescence microscopy," *Nat. Methods* **2**, 910–919 (2005).
- 395 5. X. Cao, T. Yue, X. Lin, S. Lin, X. Yuan, Q. Dai, L. Carin, and D. J. Brady, "Computational Snapshot Multispectral
396 Cameras: Toward dynamic capture of the spectral world," *IEEE Signal Process. Mag.* **33**, 95–108 (2016).
- 397 6. G. R. Arce, D. J. Brady, L. Carin, H. Arguello, and D. S. Kittle, "Compressive Coded Aperture Spectral Imaging: An
398 Introduction," *IEEE Signal Process. Mag.* **31**, 105–115 (2014).
- 399 7. Y. Oiknine, I. August, V. Farber, D. Gedalin, and A. Stern, "Compressive Sensing Hyperspectral Imaging by Spectral
400 Multiplexing with Liquid Crystal," *J. Imaging* **5**, 3 (2019).
- 401 8. K. Monakhova, K. Yanny, N. Aggarwal, and L. Waller, "Spectral DiffuserCam: Lensless snapshot hyperspectral
402 imaging with a spectral filter array," *Optica* **7**, 1298 (2020).
- 403 9. T. Sun and K. Kelly, "Compressive Sensing Hyperspectral Imager," in *Frontiers in Optics*
404 *2009/Laser Science XXV/Fall 2009 OSA Optics & Photonics Technical Digest*, (OSA, San Jose, California, 2009),
405 p. CTuA5.
- 406 10. F. Soldevila, E. Irls, V. Durán, P. Clemente, M. Fernández-Alonso, E. Tajahuerce, and J. Lancis, "Single-pixel
407 polarimetric imaging spectrometer by compressive sensing," *Appl. Phys. B* **113**, 551–558 (2013).
- 408 11. J. Peller, F. Farahi, and S. R. Trammell, "Hyperspectral imaging system based on a single-pixel camera design for
409 detecting differences in tissue properties," *Appl. Opt.* **57**, 7651–7658 (2018).
- 410 12. F. Rousset, N. Ducros, F. Peyrin, G. Valentini, C. D'Andrea, and A. Farina, "Time-resolved multispectral imaging
411 based on an adaptive single-pixel camera," *Opt. Express* **26**, 10550–10558 (2018).
- 412 13. M. P. Edgar, G. M. Gibson, and M. J. Padgett, "Principles and prospects for single-pixel imaging," *Nat. Photonics* **13**,
413 13–20 (2019).
- 414 14. G. M. Gibson, G. M. Gibson, S. D. Johnson, S. D. Johnson, M. J. Padgett, and M. J. Padgett, "Single-pixel imaging
415 12 years on: A review," *Opt. Express* **28**, 28190–28208 (2020).
- 416 15. M. Harwit and N. J. A. Sloane, *Hadamard Transform Optics* (Academic Press, 1979).
- 417 16. E. D. Nelson and M. L. Fredman, "Hadamard Spectroscopy," *JOSA* **60**, 1664–1669 (1970).
- 418 17. E. J. Candes and M. B. Wakin, "An Introduction To Compressive Sampling," *IEEE Signal Process. Mag.* **25**, 21–30
419 (2008).
- 420 18. G. Barbastathis, A. Ozcan, and G. Situ, "On the use of deep learning for computational imaging," *Optica* **6**, 921–943
421 (2019).
- 422 19. C. F. Higham, R. Murray-Smith, M. J. Padgett, and M. P. Edgar, "Deep learning for real-time single-pixel video," *Sci.*
423 *Reports* **8**, 2369 (2018).
- 424 20. S. Rizvi, J. Cao, K. Zhang, and Q. Hao, "DeepGhost: Real-time computational ghost imaging via deep learning," *Sci.*
425 *Reports* **10**, 11400 (2020).
- 426 21. A. Lorente Mur, P. Leclerc, F. Peyrin, and N. Ducros, "Single-pixel image reconstruction from experimental data
427 using neural networks," *Opt. Express* **29**, 17097–17110 (2021).
- 428 22. A. Lorente Mur, F. Peyrin, and N. Ducros, "Deep Expectation-Maximization for Single-Pixel Image Reconstruction
429 With Signal-Dependent Noise," *IEEE Transactions on Comput. Imaging* **8**, 759–769 (2022).
- 430 23. F. Wang, C. Wang, C. Deng, S. Han, and G. Situ, "Single-pixel imaging using physics enhanced deep learning,"
431 *Photonics Res.* **10**, 104 (2022).
- 432 24. Y. Tian, Y. Fu, and J. Zhang, "Plug-and-play algorithms for single-pixel imaging," *Opt. Lasers Eng.* **154**, 106970
433 (2022).
- 434 25. Y. Lu, B. Tan, S. Ding, and Y. Li, "SPI-CGAN: Single-pixel imaging based on conditional generative adversarial
435 network," *J. Physics: Conf. Ser.* **2216**, 012092 (2022).
- 436 26. L. Mahieu-William and N. Ducros, "Single-Pixel Hyperspectral Image (SPIHIM) Collection," [https://pilot-
437 warehouse.creatis.insa-lyon.fr/#collection/6140ba6929e3fc10d47dbe3e](https://pilot-warehouse.creatis.insa-lyon.fr/#collection/6140ba6929e3fc10d47dbe3e) (2022).

- 438 27. M. D. Wilkinson, M. Dumontier, I. J. Aalbersberg, G. Appleton, M. Axton, A. Baak, N. Blomberg, J.-W. Boiten, L. B.
439 da Silva Santos, P. E. Bourne, J. Bouwman, A. J. Brookes, T. Clark, M. Crosas, I. Dillo, O. Dumon, S. Edmunds, C. T.
440 Evelo, R. Finkers, A. Gonzalez-Beltran, A. J. G. Gray, P. Groth, C. Goble, J. S. Grethe, J. Heringa, P. A. C. 't Hoen,
441 R. Hooft, T. Kuhn, R. Kok, J. Kok, S. J. Lusher, M. E. Martone, A. Mons, A. L. Packer, B. Persson, P. Rocca-Serra,
442 M. Roos, R. van Schaik, S.-A. Sansone, E. Schultes, T. Sengstag, T. Slater, G. Strawn, M. A. Swertz, M. Thompson,
443 J. van der Lei, E. van Mulligen, J. Velterop, A. Waagmeester, P. Wittenburg, K. Wolstencroft, J. Zhao, and B. Mons,
444 "The FAIR Guiding Principles for scientific data management and stewardship," *Sci. Data* **3**, 160018 (2016).
- 445 28. A. Lorente Mur, T. Baudier, and N. Ducros, "Openspyrit/spyrit," openspyrit (2022).
- 446 29. G. Beneti Martins, L. Mahieu-Williams, and N. Ducros, "Single-pixel acquisition software version 1.0," (2021).
- 447 30. E. M. V. Association, "EMVA standard 1288, standard for characterization of image sensors and cameras," Release **3**,
448 29 (2016).
- 449 31. A. Lorente Mur, M. Ochoa, J. Cohen, X. Intes, and N. Ducros, "Handling negative patterns for fast single-pixel lifetime
450 imaging," in *Molecular-Guided Surgery: Molecules, Devices, and Applications V*, B. W. Pogue and S. Gioux, eds.
451 (SPIE, San Francisco, United States, 2019), p. 9.
- 452 32. P. G. Vaz, D. Amaral, L. F. R. Ferreira, M. Morgado, M. Morgado, and J. Cardoso, "Image quality of compressive
453 single-pixel imaging using different Hadamard orderings," *Opt. Express* **28**, 11666–11681 (2020).
- 454 33. A. Lorente Mur, P. Bataille, F. Peyrin, and N. Ducros, "Deep Expectation-Maximization For Image Reconstruction
455 From Under-Sampled Poisson Data," in *2021 IEEE 18th International Symposium on Biomedical Imaging (ISBI)*,
456 (IEEE, Nice, France, 2021), pp. 1535–1539.
- 457 34. S. M. Popoff and M. W. Matthès, "ALP4lib: A Python wrapper for the Vialux ALP-4 controller suite to control
458 DMDs," Zenodo (2020).
- 459 35. Measurement Standards Laboratory of New Zealand, "MSL-Equipment," .
- 460 36. H. S. Fairman, M. H. Brill, and H. Hemmendinger, "How the CIE 1931 color-matching functions were derived from
461 Wright-Guild data," *Color. Res. & Appl.* **22**, 11–23 (1997).
- 462 37. A. Paszke, S. Gross, F. Massa, A. Lerer, J. Bradbury, G. Chanan, T. Killeen, Z. Lin, N. Gimselshin, L. Antiga,
463 A. Desmaison, A. Kopf, E. Yang, Z. DeVito, M. Raison, A. Tejani, S. Chilamkurthy, B. Steiner, L. Fang, J. Bai,
464 and S. Chintala, "PyTorch: An imperative style, high-performance deep learning library," in *Advances in Neural
465 Information Processing Systems* **32**, H. Wallach, H. Larochelle, A. Beygelzimer, F. dAlché-Buc, E. Fox, and
466 R. Garnett, eds. (Curran Associates, Inc., 2019), pp. 8024–8035.
- 467 38. A. Coates, A. Ng, and H. Lee, "An Analysis of Single-Layer Networks in Unsupervised Feature Learning," in
468 *Proceedings of the Fourteenth International Conference on Artificial Intelligence and Statistics*, (JMLR Workshop
469 and Conference Proceedings, 2011), pp. 215–223.
- 470 39. J. Deng, W. Dong, R. Socher, L.-J. Li, K. Li, and L. Fei-Fei, "ImageNet: A large-scale hierarchical image database,"
471 in *2009 IEEE Conference on Computer Vision and Pattern Recognition*, (2009), pp. 248–255.
- 472 40. D. P. Kingma and J. Ba, "Adam: A method for stochastic optimization," in *3rd International Conference on Learning
473 Representations, ICLR 2015, San Diego, CA, USA, May 7-9, 2015, Conference Track Proceedings*, Y. Bengio and
474 Y. LeCun, eds. (2015).
- 475 41. A. Orych, "REVIEW OF METHODS FOR DETERMINING THE SPATIAL RESOLUTION OF UAV SENSORS,"
476 *The Int. Arch. Photogramm. Remote. Sens. Spatial Inf. Sci.* **XL-1/W4**, 391–395 (2015).
- 477 42. L. Baldassarre, Y.-H. Li, J. Scarlett, B. Gözcü, I. Bogunovic, and V. Cevher, "Learning-Based Compressive
478 Subsampling," *IEEE J. Sel. Top. Signal Process.* **10**, 809–822 (2016).
- 479 43. "AVIRIS - Airborne Visible / Infrared Imaging Spectrometer - Data," <https://aviris.jpl.nasa.gov/data/index.html>.
- 480 44. B. Arad and O. Ben-Shahar, "Sparse Recovery of Hyperspectral Signal from Natural RGB Images," in *Computer
481 Vision – ECCV 2016*, B. Leibe, J. Matas, N. Sebe, and M. Welling, eds. (Springer International Publishing, Cham,
482 2016), Lecture Notes in Computer Science, pp. 19–34.
- 483 45. V. Pronina, A. Lorente Mur, J. F. P. J. Abascal, F. Peyrin, D. V. Dylov, and N. Ducros, "3D denoised completion
484 network for deep single-pixel reconstruction of hyperspectral images," *Opt. Express* **29**, 39559 (2021).